Tuijin Jishu/Journal of Propulsion Technology
ISSN: 1001-4055
Vol. 45 No. 2 (2024)

Williamson Fluid Characteristics on Three-Dimensional Steady Nanofluid Flow Past a Bi-Directional Stretching Sheet: Double Diffusion and MHD Effects

K. G. R. Deepthi[1,*], S. Kavitha[2], and V. Vasudeva Murthy[3]

[1]*Department of Mathematics, Vishnu Institute of Technology, Bhimavaram, West Godavari, 534302, Andhra Pradesh, India*

[2]*Department of Mathematics, Annamalai University, Annamalai Nagar, 608002, Tamilnadu State, India*

[3]*Department of Mathematics, S. R. K. R. Engineering College, Bhimavaram, West Godavari, 534201, Andhra Pradesh, India*

Abstract: The goal of this study is to determine how heat radiation and chemical reactions affect a non-Newtonian Williamson-nanofluid flow across a stretched sheet in a porous media. There will be no compressibility, consistent viscosity, or three-dimensionality to the flow. Applying the finite element approach yields the system's approximate solutions to its partial differential equations. For many important parameter values, the graphical representations of the concentration, velocity, temperature, mass, heat transfer rate, and shear stresses of Williamson nanofluids at the stretched sheet are provided. On top of it, the shear stresses are shown. Finally, the results show that the previous study and the comparison inquiry are very much in accord.

Keywords: Williamson fluid; Nanofluid; Three-dimensional steady flow; MHD; Chemical reaction; Numerical Solutions; Bi-directional stretching sheet;

1. Introduction:

Fluid mechanics research includes non-Newtonian fluids. A non-Newtonian fluid's thickness and flow resistance may change as a consequence of a change in viscosity caused by an external force. Non-Newtonian fluids are defined as Williamson fluids due to their shear-thinning and thickening properties. The shear stress rate has a significant effect on the Williamson fluid viscosity, which drops dramatically as it rises [3]. There are several important applications for Williamson fluids, including lubricants, emulsions, biological fluids, and nuclear fuel slurries. Scientists have poured a lot of time and energy into studying Williamson fluid ([1],[2],[4]-[6]) because of its unique properties and many uses. Hashim et al. [7] studied the Williamson fluids (which showed transient flow with the heat transmission mechanism) and their variable thermal conductivity. Growing exponentially with time is the Williamson fluid flow viscosity. This research by Salhuddin et al. [8] investigated the effects of induced magnetohydrodynamics (MHD). Diffusivity and conductivity were studied at different scales. As an example, Bouslimi et al. [9] looked at how Joule heating affected the flow characteristics of a Williamson nanofluid in a porous medium. In order to explain the increased wall friction, the researchers stressed that a higher Darcy number and magnetic field parameter may be responsible. Two scholarly investigations [10] and [11] looked at how Joule heating affected the Williamson nanofluid's flow along a long, cylindrical surface. Hayat et al. [12] studied convective heat and mass transport in Williamson nanofluid flow. According to the study's findings, temperature and concentration Biot numbers stimulated the development of concentration and temperature profiles. It was through their inquiry that this finding was made. Rashad et al. [13] checked into how temperature affects the flow of Williamson hybrid nanofluids on a curved surface in convective situations. Radiation heat has many practical uses, but it is especially important in gas turbines, spacecraft, airplanes, and satellite propulsion systems. A large number of research are thus looking at how radiative heat transfer affects

nanofluid technology ([14]-[19]). When a cross-fluid flowed across a surface that extended vertically, Manzur et al. [20] measured the combined convective heat. In their analysis, the researchers took into account buoyancy factors that worked in tandem with or against buoyancy. In their investigation of the fluid dynamics around a spinning disk, Qayyum et al. [21] aimed to determine the effect of thermal radiation on a combination of nanoparticles and microbes. Nanofluid flow in carbon nanotubes under partial slip boundary conditions was computationally studied by Hayat et al. in relation to radiation. [22]. Shoaib et al. [23] state that hybrid nanofluids are investigated as they travel around a revolving disk in three dimensions. Viscosity dissipation, joule heating, nonlinear thermal radiation, and joule heating all interact in a suitable way. For their investigation, Nuwairan and Souayeh [24] used electromagnetic-hydrodynamic (EMHD) microchannel blood flow to identify the impact of gold nanoparticles. Gyrotactic bacteria, radiation, activation energy, and bioconvection were all factors that the researchers sought to understand in relation to blood circulation. Aman et al. [25] researched the matter by looking at how heat radiation affects Poiseuille mixed convection. The impact of thermal radiation on the uncontrolled nanofluid flow in an unstructured environment was studied by Mostafazadeh et al. [26] using computational methods. The goal of this research is to see how a Williamson fluid near a stretched sheet with nanofluid particles behaves when magnetohydrodynamics (MHD) and double diffusion are applied together. Durgarao et al. Studied the combined impact of thermophoresis and Brownian motion on the Willamson-nano fluid flow near a non-linear stretching sheet filled by porous medium. Finally, the consequences of heat radiation, chemical interactions, and porous materials are taken into account. Based on the previous study questions, the current investigation was conducted. Distinctive to this study is its examination of the interplay between the pace of disturbance development and chemical reactions, thermal diffusion, and diffusion thermo effects. The following is a schedule of the contents of this document: Part 2 provides a detailed description of the flow materials' geometric properties, while Section 3 examines the formulation and numerical approach in great detail. In Section 4, we lay out the whole procedure for validating the code. The numerical findings and an analysis make up the fifth portion. Section six finally provides a conclusion.

2. Flow Governing Equations:

This research delves at the interplay between thermal radiation and magnetic fields as they pertain to a three-dimensional, non-Newtonian Williamson fluid flow characterized by incompressibility, viscosity, chemical reactivity, and electrical conductivity all at once. A bidirectionally expanding porous media sheet allows the flow to pass through, taking into consideration both thermophoresis and Brownian motion effects. Figure 1 shows the physical geometry of the fluid route. In order to facilitate this inquiry, we assume the following:

i. The x and y coordinates of the sheet's velocities are assumed to be $U_w(x) = ax$ and $V_w(y) = by$, respectively.

ii. A B_o -strong magnetic field exerts an influence on the flux being examined in this research.

iii. The energy equation does not take everything into consideration, including ohmic heating, joule heating, viscous dissipation, and heat source.

iv. Assumptions concerning Brownian motion, thermal radiation, and thermophoresis are also incorporated into the energy equation.

v. Double diffusion is not accounted for in thermal and energy calculations.

vi. In determining the concentration of a given species, the influence of the chemical reaction is further taken into account.

section

vii. To begin, let's pretend that $T_w$and $C_w$are the interface's temperature and concentration constants, and that $T_\infty$and C_∞ are the free stream fluid's temperature and concentration beyond the thermal boundary layer.

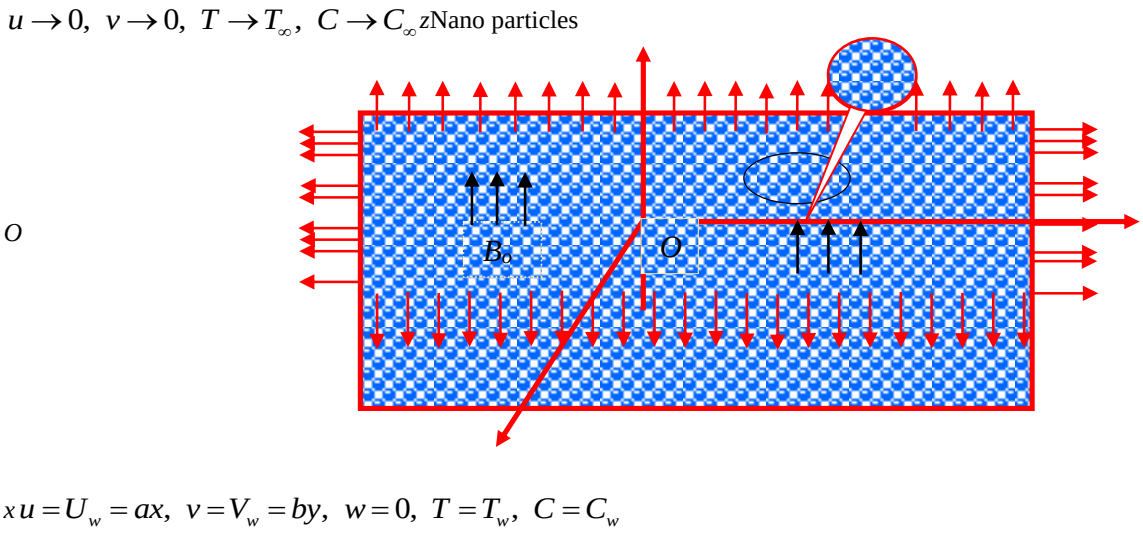

Fig. 1.: The movement of a Williamson-Nanofluid towards a stretched sheet

The fundamental equations that regulate Williamson-Nanofluid flow, supposing the aforementioned, are

The Equation of Continuity:

$$\frac{\partial u}{\partial x}+\frac{\partial v}{\partial y}+\frac{\partial w}{\partial z}=0 \tag{1}$$

The Equation of Momentum:

$$u\left(\frac{\partial u}{\partial x}\right)+v\left(\frac{\partial u}{\partial y}\right)+w\left(\frac{\partial u}{\partial z}\right)=\frac{\partial^2 u}{\partial z^2}+\sqrt{2}\Gamma\left[\frac{\partial u}{\partial z}\right]\left[\frac{\partial^2 u}{\partial z^2}\right]-\left(\frac{\sigma B_o^2}{\rho}\right)u-\nu\left(\frac{u}{k_1}\right), \tag{2}$$

$$u\left(\frac{\partial v}{\partial x}\right)+v\left(\frac{\partial v}{\partial y}\right)+w\left(\frac{\partial v}{\partial z}\right)=\frac{\partial^2 v}{\partial z^2}+\sqrt{2}\Gamma\left[\frac{\partial v}{\partial z}\right]\left[\frac{\partial^2 v}{\partial z^2}\right]-\left(\frac{\sigma B_o^2}{\rho}\right)v-\nu\left(\frac{v}{k_1}\right), \tag{3}$$

Equation of thermal energy:

$$u\left(\frac{\partial T}{\partial x}\right)+v\left(\frac{\partial T}{\partial y}\right)+w\left(\frac{\partial T}{\partial z}\right)=\alpha\left(\frac{\partial^2 T}{\partial z^2}\right)+\left(\frac{(\rho C)_p}{(\rho C)_f}\right)\left\{D_B\left(\frac{\partial T}{\partial z}\right)\left(\frac{\partial C}{\partial z}\right)+\frac{D_T}{T_\infty}\left(\frac{\partial T}{\partial z}\right)^2\right\}-\frac{1}{\rho C_p}\left(\frac{\partial q_r}{\partial z}\right) \tag{4}$$

Equation of species Concentration:

$$u\left(\frac{\partial C}{\partial x}\right)+v\left(\frac{\partial C}{\partial y}\right)+w\left(\frac{\partial C}{\partial z}\right)=D_B\left(\frac{\partial^2 C}{\partial z^2}\right)+\frac{D_T}{T_\infty}\left(\frac{\partial T}{\partial z}\right)^2-Kr\left(C-C_\infty\right) \tag{5}$$

This flow is subject to the following boundary conditions:

$$\left.\begin{aligned} &u = U_w = ax,\ v = V_w = by,\ w = 0,\ T = T_w,\ C = C_w \ \ at\ \ z = 0 \\ &u \to 0,\ v \to 0,\ T \to T_\infty,\ C \to C_\infty \ \ as\ \ z \to \infty \end{aligned}\right\} \tag{6}$$

The radiative heat flow q_r is equal to, as per the Roseland approximation

$$q_r = -\frac{4\sigma^*}{3K^*}\left(\frac{\partial T^4}{\partial z}\right) \tag{7}$$

For the sake of argument, let's pretend that the temperature variations inside the flow are linearly related to the term T^4. To do this, we may use the following expansion of T^4 in a Taylor series around a free-stream temperature T_∞:

$$T^4 = T_\infty^4 + 4T_\infty^3\left(T - T_\infty\right) + 6T_\infty^2\left(T - T_\infty\right)^2 + \ldots\ldots\ldots \tag{8}$$

Stepping back from the preceding equation and excluding terms of a higher order than the first degree in $\left(T - T_\infty\right)$, we get

$$T^4 \cong 4T_\infty^3 T - 3T_\infty^4 \tag{9}$$

Hence, by plugging Equation. (9) into Equation. (7), we get

$$q_r = -\frac{16T_\infty^3\sigma^*}{3K^*}\left(\frac{\partial T}{\partial z}\right) \tag{10}$$

Equation (3) may be expressed as follows by using (8):

$$u\left(\frac{\partial T}{\partial x}\right) + v\left(\frac{\partial T}{\partial y}\right) + w\left(\frac{\partial T}{\partial z}\right) = \alpha\left(\frac{\partial^2 T}{\partial z^2}\right) + \left(\frac{(\rho C)_p}{(\rho C)_f}\right)\left\{D_B\left(\frac{\partial T}{\partial z}\right)\left(\frac{\partial C}{\partial z}\right) + \frac{D_T}{T_\infty}\left(\frac{\partial T}{\partial z}\right)^2\right\} + \frac{1}{\rho C_p}\left(\frac{16T_\infty^3\sigma^*}{3\kappa k^*}\right)\left(\frac{\partial^2 T}{\partial z^2}\right) \tag{11}$$

Starting the subsequent modifications based on similarities

$$\left.\eta = \left(\sqrt{\frac{a}{\nu}}\right)z,\ \ u = axf'(\eta),\ v = ayg'(\eta),\ \theta = \frac{T - T_\infty}{T_w - T_\infty},\ \phi = \frac{C - C_\infty}{C_w - C_\infty},\ w = \nu\sqrt{\nu a}\left\{f(\eta) + g(\eta)\right\},\ \right\} \tag{12}$$

Equation (1), when combined with Equation (12), is represented as follows in Equations (2), (3), (4), and (11).

$$f''' - f'^2 + ff'' + gf'' - Mf' - Kf' + \lambda f''\,f''' = 0 \tag{13}$$

$$g''' - g'^2 + fg'' + gg'' - Mg' - Kg' + \lambda g''g''' = 0 \tag{14}$$

$$\left\{\frac{d}{d\eta}\left[\left(1 + Rd\left(1 + \left(\theta_w - 1\right)\theta\right)^3\right)\theta'\right]\right\} + \Pr\, f\theta' + \Pr\, g\theta' + \Pr\, Nb\theta'\phi' + \Pr\, Nt\theta'^2 = 0 \tag{15}$$

$$Nb\phi'' + NbScf\,\phi' + NbScg\phi' + Nt\theta'' - ScNb\gamma\phi = 0 \tag{16}$$

the corresponding boundary conditions (6) becomes

$$\left.\begin{aligned} &f(0) = 0,\ \ g(0) = 0,\ \ f'(0) = 1,\ \ g'(0) = \beta,\ \ \theta(0) = 1,\ \ \phi(0) = 1, \\ &f'(\infty) \to 0,\ \ g'(\infty) \to 0,\ \ \theta(\infty) \to 0,\ \ \phi(\infty) \to 0 \end{aligned}\right\} \tag{17}$$

under what circumstances are the relevant physical properties described as

$$\left.\begin{aligned} M=\frac{\sigma B_o^2}{\rho U_o},\ \beta=\frac{b}{a},\ \theta_w=\frac{T_w}{T_\infty},\ Nb=\frac{\tau_B D_B\left(C_w-C_\infty\right)}{\nu},\ K=\frac{\nu}{ak_1},\ \gamma=\frac{Kr}{a},\\ Nt=\frac{\tau_B D_T\left(T_w-T_\infty\right)}{\nu T_\infty},\ Sc=\frac{\nu}{D_B},\ Rd=\frac{16\sigma^* T_\infty^3}{3\kappa k^*},\ \Pr=\frac{\nu}{\alpha},\ \lambda=\Gamma x\sqrt{\frac{2a^3}{\nu}},\end{aligned}\right\}$$

(18)

This is the *x* and *y*-dimensional portrayal of important physical values, local Sherwood and Nusselt numbers, and skin-friction coefficient physical properties:

$$Cf_x=\frac{\tau_{wx}}{\rho U_w^2}=-\frac{\mu}{\rho U_w^2}\left(\frac{\partial u}{\partial z}+\frac{\Gamma}{\sqrt{2}}\left(\frac{\partial u}{\partial z}\right)^2\right)_{z=0}\Rightarrow\left(\sqrt{\mathrm{Re}_x}\right)Cf_x=-f''(0)\left(1+\frac{\lambda}{2}f''(0)\right)$$

(19)

$$Cf_y=\frac{\tau_{wy}}{\rho U_w^2}=-\frac{\mu}{\rho U_w^2}\left(\frac{\partial v}{\partial z}+\frac{\Gamma}{\sqrt{2}}\left(\frac{\partial v}{\partial z}\right)^2\right)_{z=0}\Rightarrow\left(\sqrt{\mathrm{Re}_y}\right)Cf_y=-g''(0)\left(1+\frac{\lambda}{2}g''(0)\right)$$

(20)

$$Nu=\frac{xq_w}{\kappa\left(T_w-T_\infty\right)}=-\frac{x\left(\frac{\partial T}{\partial z}+\frac{\partial q_r}{\partial z}\right)_{z=0}}{\kappa\left(T_w-T_\infty\right)}\Rightarrow Nu=-\left(1+Rd\,\theta_w^3\right)\left(\sqrt{\mathrm{Re}_x}\right)\theta'(0)$$

(21)

$$Sh=\frac{xq_m}{D_B\left(C_w-C_\infty\right)}=-\frac{x\left(\frac{\partial C}{\partial z}\right)_{z=0}}{D_B\left(C_w-C_\infty\right)}\Rightarrow Sh=-\left(\sqrt{\mathrm{Re}_x}\right)\phi'(0)$$

(22)

The local Reynolds numbers, denoted as $\mathrm{Re}_x=\frac{U_w x}{\nu}$ and $\mathrm{Re}_y=\frac{V_w y}{\nu}$, respectively, are determined by the stretching velocities, $U_w(x)$ and $V_w(y)$.

3. Method of Solution by Finite Element Method:

The finite element method must be used when resolving both partial and ordinary differential equations. Differential equation solutions become simple when this method is used. The partition of the domain into smaller, finite-dimensional units known as finite elements is the foundation of the finite element approach. This method represented the most flexible and all-around strategy to doing engineering studies at the time this publication was written. This method has been used to exams in numerous academic subjects, including rigid body dynamics, electrical systems, acoustics, heat transfer, solid mechanics, and chemical processes. Figure 2 shows the application of the finite element approach. Prior to beginning a finite element analysis, ensure that the following have been fully fulfilled:

- **Domain discretization into elements:** In order to implement discretization via finite elements, the entire interval is subdivided into an elemental number of smaller intervals.
- **Domain breakdown into elements:** All of the previously outlined components make up the finite-element mesh.
- When formulating equations using elements, follow these steps:

a) The initial adjustments to the mathematical model are based on the standard element, which is a single mesh element.

b) A previously created system is used to solve the variational issue for the variable, and when an approximate solution is found, the element equations are formed by plugging in the estimated response.

c) The rigidity matrix, or just the matrix generated by interpolating polynomials, is another name for this.

- **Construction and solution of equations:** In order to construct an algebraic equation in its entirety, each element's section must adhere to constraints on inter-element continuity. A global finite-element model of the entire domain can be constructed through the fusion of a substantial number of algebraic equations.
- **Applying boundary conditions:** The resulting equations need to be corrected according to the flow model's boundary requirements.

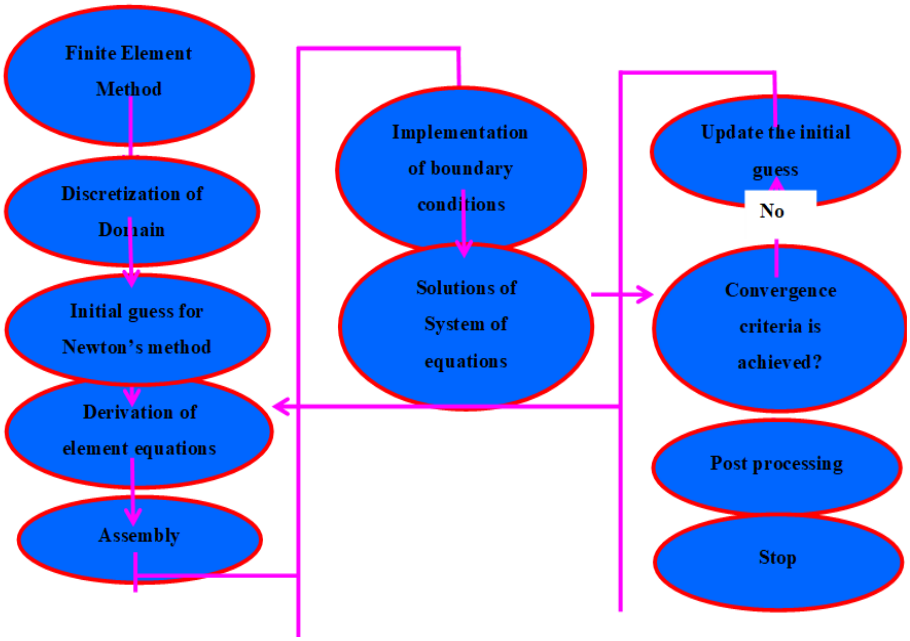

Fig. 2.Flow chart for the Finite Element Technique

It is possible to solve built equations using a wide variety of numerical methods, such as the LU decomposition method and the Gauss elimination approach. Remembering the form functions used to approximation real functions is crucial when dealing with real numbers. The twenty thousand nodes that make up the flow domain are all quadratic components of the same magnitude. In the domain of flow, the magnitudes of the 10,000 quadratic components are similar. A set of 80.04 nonlinear equations may be analyzed when the element equations were formulated. The residual system of nonlinear equations is numerically solved to an accuracy of 0.00001 using the Gauss elimination technique after boundary constraints are imposed. In order to solve integration difficulties, the Gaussian quadrature might be used. The operation was carried out using a desktop computer that ran MATHEMATICA.

4. Program Code Validation:

Table-1.: Examining the current numerical results in relation to the published findings of Liu and Anderson [25] for various values of β at Pr = 1.0 when $M = 0$, $K = 0$, $\lambda = 0$, $Nb = 0$, $Nt = 0$, $Rd = 0$, and $\gamma = 0$.

β	Present numerical results			Results of Liu and Anderson [25]		
	$-f''(0)$	$-g''(0)$	$-\theta'(0)$	$-f''(0)$	$-g''(0)$	$-\theta'(0)$
0.25	1.0477687934	0.1897787847	0.6576767033	1.048813	0.194565	0.665933
0.50	1.0858098786	0.4596789823	0.7289667690	1.093096	0.465206	0.735334
0.75	1.1289782245	0.7866780303	0.7896659203	1.134486	0.794619	0.796472

In Table 1, the authors compare the numerical findings with those reported by Liu and Anderson [27] for various values of β at Pr = 1.0. By doing this comparison, we can further confirm that our numerical results are in excellent agreement with the published data.

5. Results and Discussion:

To determine the patterns of concentration, motion, and temperature, several physical factors have been tested with different values. There is a great deal of interest.

- As seen in Figures 3 and 4, the velocity patterns along the x and y axes are affected by the magnetic field attributes (M). Studies have shown that velocity fields get smaller with larger values of M. Since the fluid's motion is slowed down by a magnetic field, the thickness of the boundary layers separating momentum and velocity contracts.
- Each of the three figures (5 and 6) displays how the permeability measure changes the main and secondary motion patterns. Based on early theoretical results, it looks like velocity profiles and the porosity measure K are linked in the opposite way. More porosity leads to slower velocity rates. Because the thin layer is expanding and the momentum barrier layer is getting thicker, K goes up.
- The graphical impacts of the Williamson parameter (λ) on the main and secondary velocity profiles, respectively, are shown in Figures 7 and 8, which include commentary. Drawing numerical values for the Williamson parameter (ξ) from these numbers reduces the fluid velocity. Viscosity profiles are reduced due to the direct relationship between relaxation time and the Williamson parameter λ.
- When looking at secondary velocity profiles, Figure 9 shows how the velocity ratio parameter (β) behaves. Figure shows that secondary velocity profiles likewise show an increasing trend as the values of the velocity ratio parameters grow.
- Figure 10 shows how the Prandtl number could change as a function of temperature. Wearing off of the thermal boundary layer is shown to occur with increasing Prandtl numbers. Increases in the Prandtl number cause fluids to have a lower thermal diffusivity, which further reduces the temperature.
- Figure 11 shows the changes introduced to the temperature profile as a result of higher Rd values. Since the presence of Rd boosts the conduction effect of the nanofluid, it is shown that the fluid temperature rises as Rd increases. So, the boundary layer area will become hotter when Rd values are high, which means surface heat flow is much higher.
- The concentration and temperature curves that match the Brownian motion measure (Nb) can be seen in Figures 12 and 13. The edges of the plots show that increasing the Brownian motion parameter makes the thermal boundary layer stand out more and the difference in surface temperature less noticeable. When the Brownian motion value goes up, on the other hand, there is a clear pattern of difference in the concentration curves and border layer width.
- As seen in Figures 14 and 15, the thermophoresis parameter (Nt) has an effect on the concentration profile, whereas Figure 15 shows the temperature profile. Looking at the data, it seems like a more seamless transition between temperature and concentration should happen when the thermophoresis parameter is raised.

Table-3.:Coefficient of skin friction in the x-direction

M	K	λ	β	Pr	Rd	Nb	Nt	θ_w	Sc	γ	Cfx
0.1	0.3	0.5	0.5	0.71	0.5	0.3	0.5	0.5	0.22	0.5	1.8678369834
0.3											1.8240472162
0.5											1.8078978216
	0.5										1.8309709813
	0.7										1.8199875295
		1.0									1.8256987062
		1.5									1.7917609873
			0.8								1.8856671436
			1.0								1.9078087126
				1.00							1.8397756876
				3.00							1.8115609364
					1.0						1.8809857995
					1.5						1.9016587683

						0.5					1.8876500315
						0.8					1.9069060391
							0.8				1.8998756875
							1.2				1.9175387467
								1.0			1.8963650613
								1.5			1.9176989826
									0.30		1.8376842982
									0.66		1.8065083760
										1.0	1.8210670987
										1.5	1.8016403745

- The value θ_w for the temperature ratio has an effect on the temperature distribution, as shown in Figure 16. A stronger thermal boundary layer and higher temperatures are both indicated by θ_w readings that are higher. This is elaborated about below. Energy Equation (15) is plainly comparable to the effective thermal diffusivity, which is determined by multiplying the radiation effect thermal diffusivity with the classical thermal diffusivity (α). One would expect that the parameter θ_w, which represents the coefficient of the second term, would provide evidence for the thermal boundary layer's thickness. In addition, the unusual *S*-shaped form that the profiles take on as θw becomes stronger strongly suggests an adiabatic scenario. That is to say, with sufficiently large mass-to-ambient temperature ratios, the wall temperature gradient basically approaches zero.

Table-4.: Skin-friction coefficient numbers are shown on the y-axis.

M	*K*	*λ*	*β*	Pr	*Rd*	*Nb*	*Nt*	θ_w	*Sc*	*γ*	*Cfy*
0.1	0.3	0.5	0.5	0.71	0.5	0.3	0.5	0.5	0.22	0.5	0.7578905903
0.3											0.7316743721
0.5											0.7197676234
	0.5										0.7245627868
	0.7										0.7076809270
		1.0									0.7316760374
		1.5									0.7196593609
			0.8								0.7835201658
			1.0								0.8023058410
				1.00							0.7248301598
				3.00							0.6953024870
					1.0						0.7820135687
					1.5						0.8036015901
						0.5					0.7765707303
						0.8					0.7908956798
							0.8				0.7967894534
							1.2				0.8178842523
								1.0			0.7817698679
								1.5			0.8008769873
									0.30		0.7103487938
									0.66		0.3886780983
										1.0	0.7116904393
										1.5	0.6905679339

- In Figure 17, we can see how the Schmidt number (*Sc*) affects concentration patterns. Finding the Sc value is as simple as dividing the mass diffusivity by the momentum. Use of diffusion in the concentration (species)

boundary layer allows comparison of momentum and mass transfer. As *Sc* is increased, the mass diffusivity of the fluid is decreased, leading to a dip in concentration profiles. Sc concentrations are inversely related to mass diffusivity, meaning that lower concentration boundary layers are linked to greater Sc concentrations.

- Image 18 shows how the chemical reaction parameter (γ) changes the patterns of concentration. Pictures show that the concentration profiles of the flow go down as the chemical reaction parameter goes up.

Table-5.: The heat transfer coefficient rate results

Pr	*Rd*	*Nb*	*Nt*	θ_w	Nu_x
0.71	0.5	0.1	0.3	0.5	0.6576073034
1.00					0.6276798679
7.00					0.6078787193
	1.0				0.6897864096
	1.5				0.7053657631
		0.3			0.6863760134
		0.5			0.7179879341
			0.6		0.6907798375
			0.8		0.7263290913
				1.0	0.6767984766
				1.5	0.6909874498

Table-6.: Findings for the mass transfer coefficient at a rate

Nt	*Nb*	*Sc*	γ	Sh_x
0.3	0.1	0.22	0.5	0.8969691739
0.6				0.9267879453
0.8				0.9416587345
	0.3			0.8567987614
	0.5			0.8318751645
		0.30		0.8669309134
		0.78		0.8466676316
			1.0	0.8692698346
			1.5	0.8434139867

- According to Tables 2 and 3, the factors *M*, λ, *K*, β, Pr, *Rd*, *Nb*, *Nt*, *Sc*, θ_w, and γ are numbers that represent the Skin-friction coefficients in the *x* and *y* planes. According to the tables, when γ,*Rd*, *Nb*, *Nt*, and β go up, so do the corresponding skin-friction factors in the x and y directions. As λ, *M*, *K*, λ, *Pr*, *Sc*, and γ go up, they show a decrease.
- For various values of *Pr*, *Rd*, *Nb*, *Nt*, and θ_w, Table 4 displays the nusselt number (Nu_x), which represents the rate of heat transfer coefficient. The rate of heat transport increases in tandem with increases in *Rd*, *Nb*, *Nt*, andθ_w. Conversely, if *Pr* increases, the converse occurs.
- Table 5 shows the impacts of *Nb*, *Nt*, *Sc*, and γ on the Sherwood number (Sh_x), which is a name for the mass transfer coefficient rate. A decrease in the mass transfer coefficient rate is seen when *Nt* increases, as shown in the table. But it increases when the numbers of *Nb*, *Sc*, and γ increase.

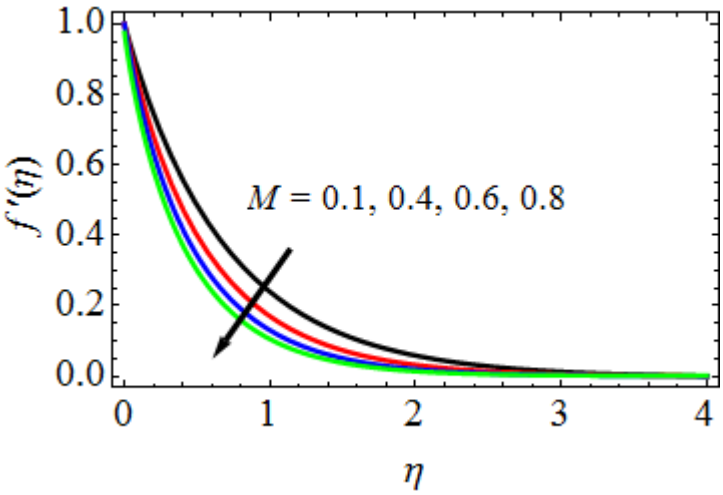

Fig. 3. How M influences velocity profiles in the *x*-direction

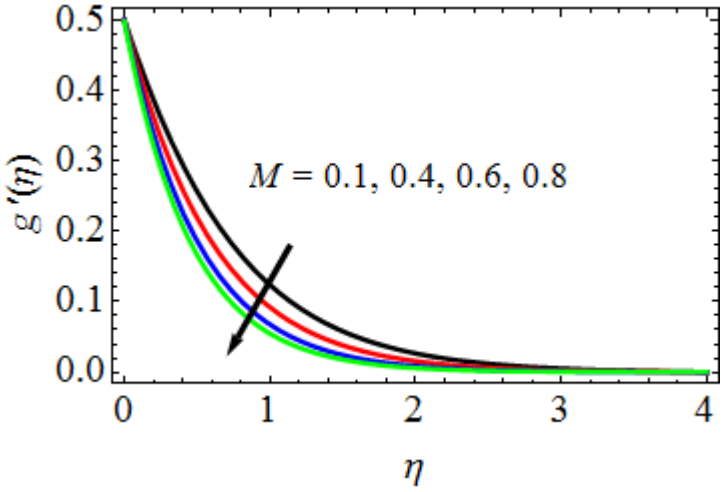

Fig. 4.How M influences velocity profiles in the *y*-direction

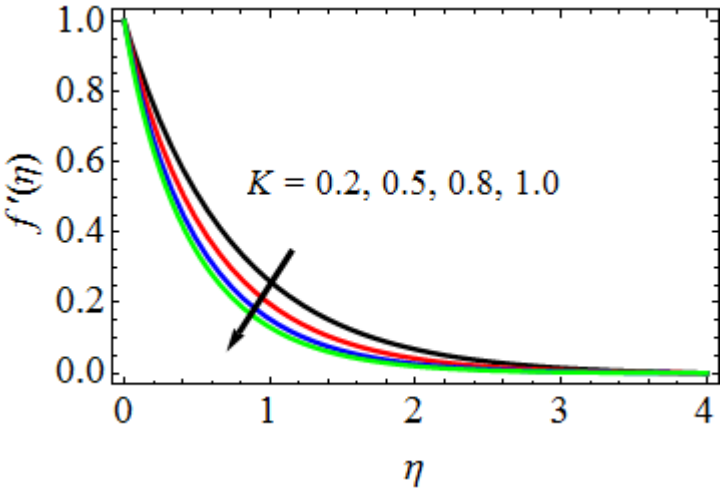

Fig. 5. How *K* influences velocity profiles in the *x*-direction

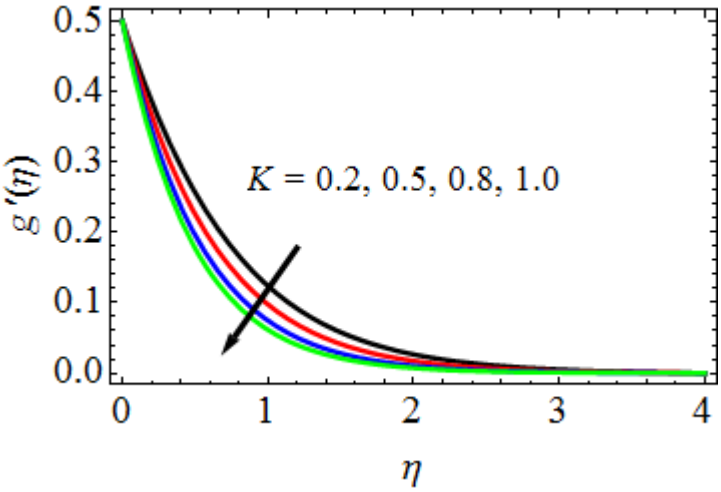

Fig. 6. How *K* influences velocity profiles in the *y*-direction

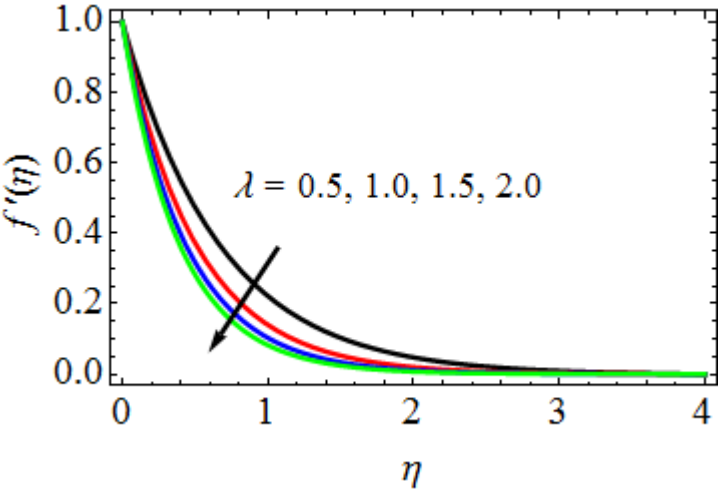

Fig. 7. How λ influences velocity profiles in the *x*-direction

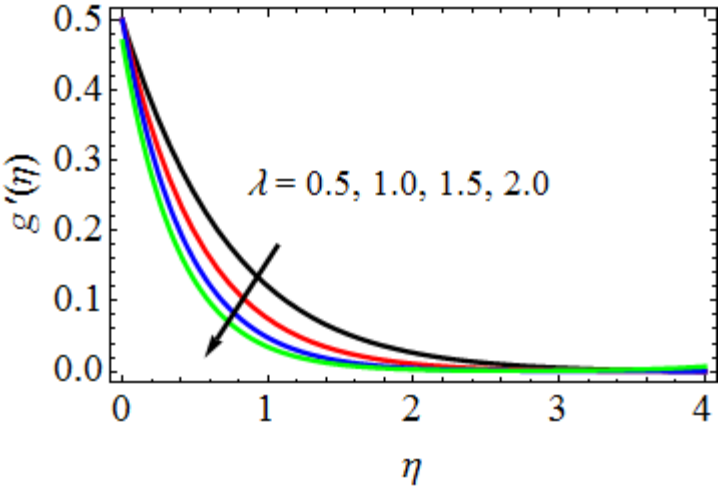

Fig. 8.How λ influences velocity profiles in the *y*-direction

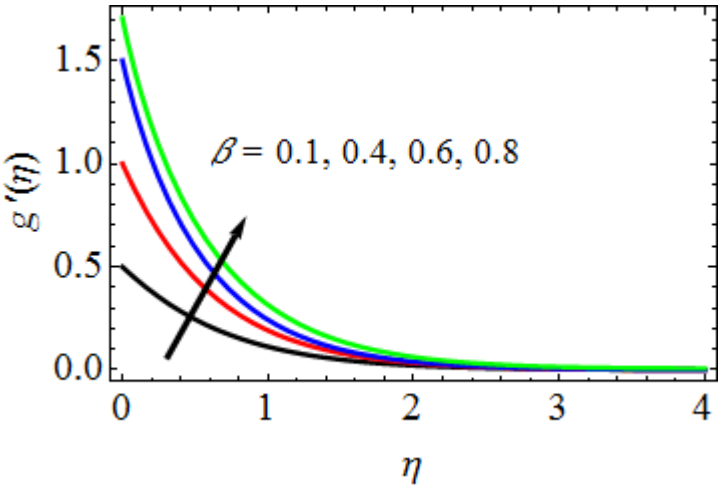

Fig. 9. How *β* influences velocity profiles in the *y*-direction

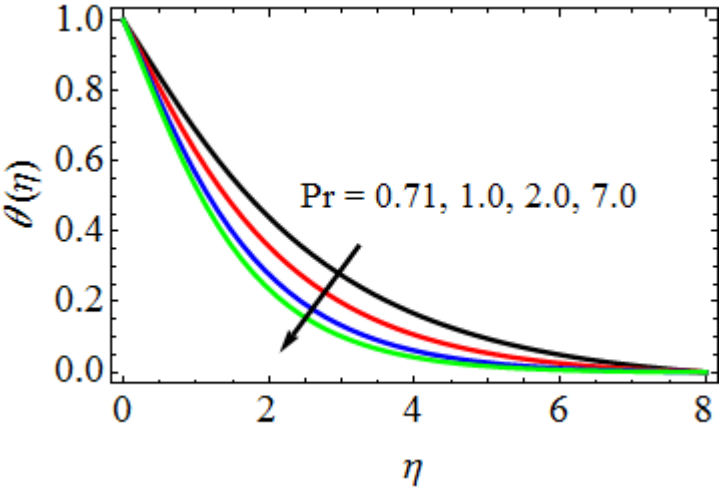

Fig. 10.The influence that *Pr* has on temperature profiles

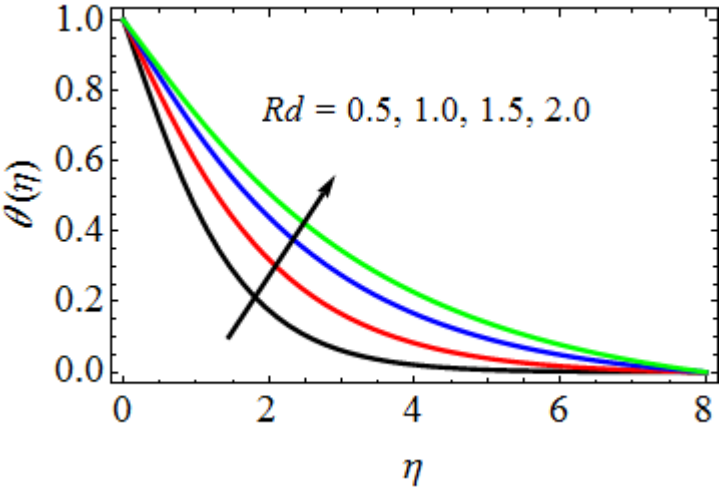

Fig. 11.The influence that *Rd* has on temperature profiles

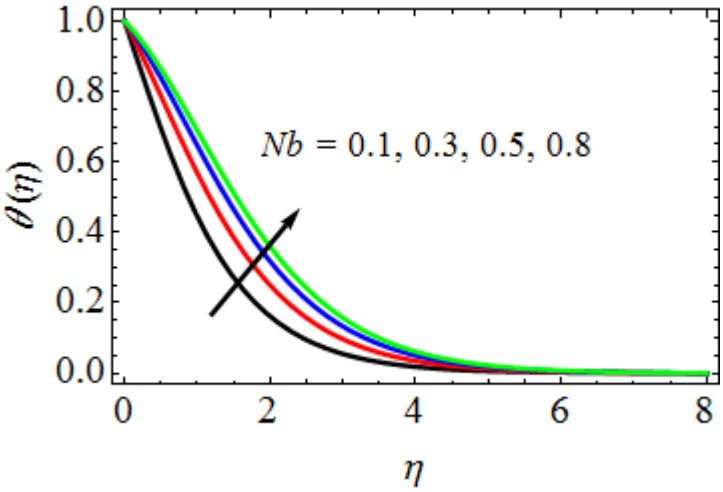

Fig. 12. The influence that *Nb* has on temperature profiles

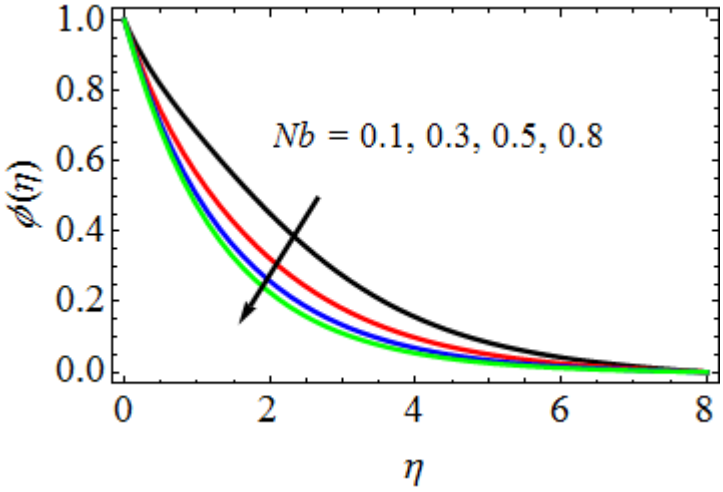

Fig. 13. The influence that *Nb* has on concentration profiles

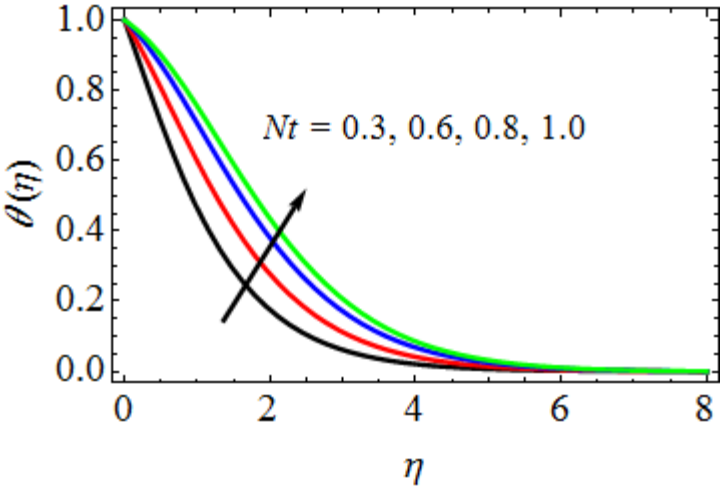

Fig. 14. The influence that *Nt* has on temperature profiles

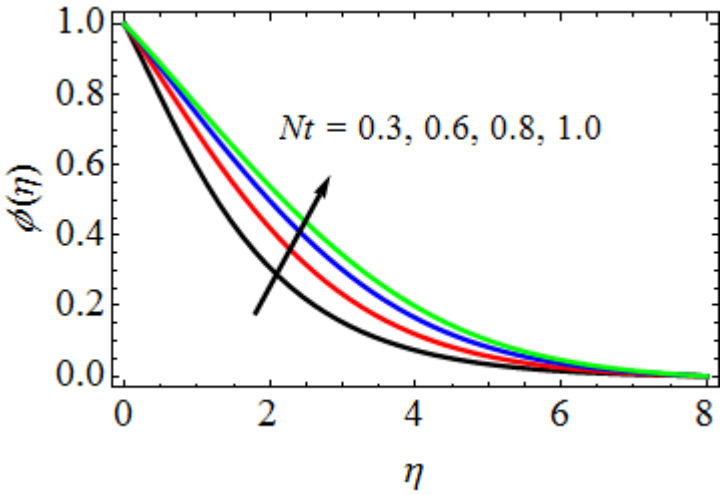

Fig. 15. The influence that *Nt* has on concentration profiles

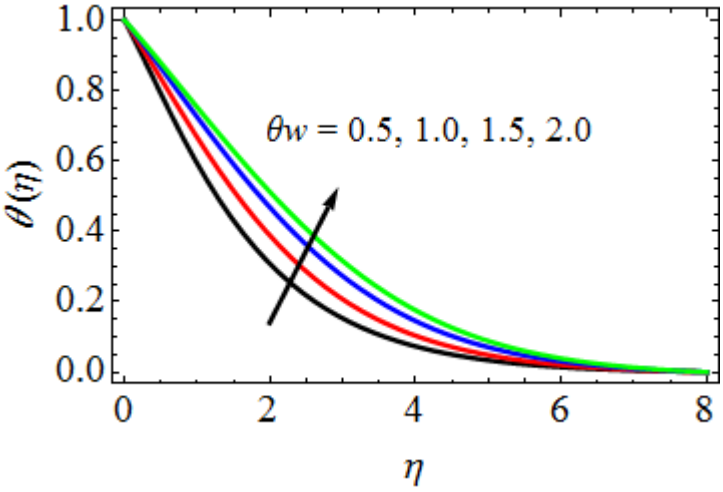

Fig. 16. The influence that *θw* has on temperature profiles

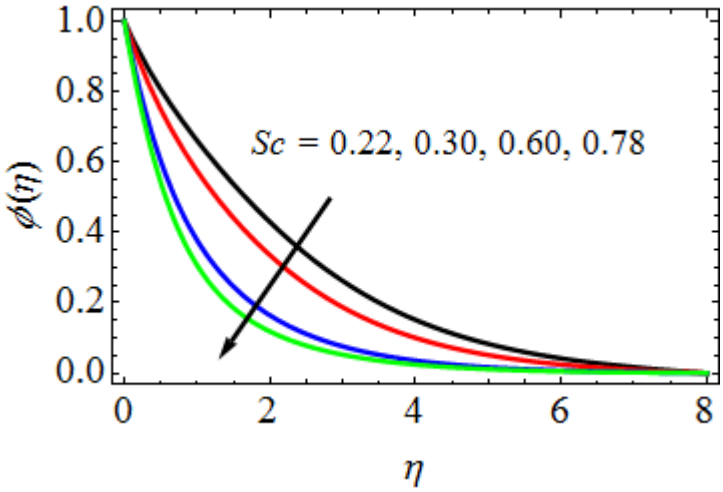

Fig. 17. The influence that *Sc* has on concentration curves

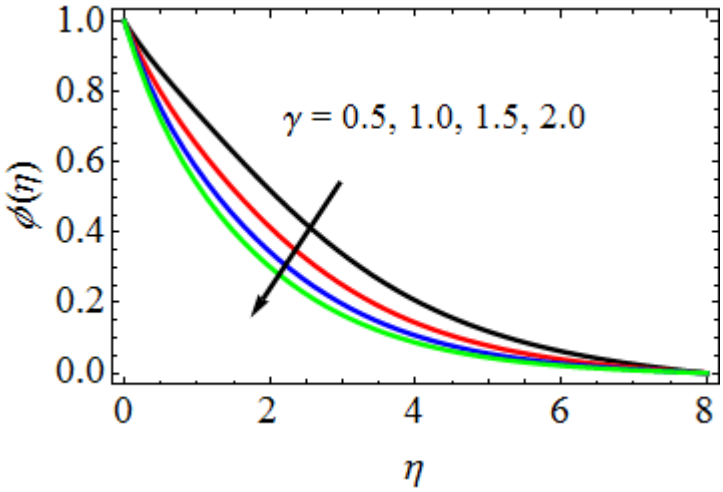

Fig. 18. The influence of γ on concentration charts

- In Tables 2 and 3, we can see the values of the skin friction coefficients in the x and y directions for *M*, λ, *K*, β, *Pr*, *Rd*, *Nb*, *Nt*, *Sc*, θ_w, and γ, respectively. According to the tables, the skin-friction coefficients in the x and y directions are increased by the values of β, *Rd*, *Nb*, *Nt*, and θ_w. When *M*, *K*, λ, *Pr*, *Sc*, and γ are increased, these coefficients are decreased. You can find the nusselt number (Nu_x), sometimes called the rate of heat transfer coefficient, for different values of *Pr*, *Rd*, *Nb*, *Nt*, and θ_w in Table 4. The rate of heat transfer coefficient increases with the values of *Rd*, *Nb*, *Nt*, and θ_w, as shown in the table. On the other hand, *Pr* has the reverse impact. The relationship between the Sherwood number (Sh_x) or rate of mass transfer coefficient and *Nb*, *Nt*, *Sc*, and γ is examined in Table 5, which displays the results in tabular fashion. According to this table, the mass transfer coefficient rate rises with increasing *Nt*, but falls with increasing *Nb*, *Sc*, and γ.
- Between *x* and *y*, Tables 2 and 3 show the numbers for skin friction coefficients. It has *M*, λ, *K*, β, *Pr*, *Rd*, *Nb*, *Nt*, *Sc*, θ_w, and γas factors. We can see from the tables that the *x* and *y* directions of the skin-friction factors get bigger as β, *Rd*, *Nb*, *Nt*, and θw get bigger as well. These factors get smaller as *M*, *K*, λ, *Pr*, *Sc*, and γ get bigger. From Table 4, we can see the values of *Pr*, *Rd*, *Nb*, *Nt*, and θ_w that are related to the nusselt number (Nu_x), which is also called the rate of heat transfer coefficient. Like the graph shows, *Rd*, *Nb*, *Nt*, and $\theta_w$all go up as the heat transfer coefficient goes up. At the same time, the opposite is true for Pr. It was found that *Nb*, *Nt*, *Sc*, γ, and the rate of mass transfer coefficient (Sh_x), which is shown in Table 5, are all related. The mass transfer coefficient rate goes up as *Nt* goes up, but down as *Nb*, *Sc*, and γ go down.

6. Conclusions:

This work studies the characteristics of a viscous Williamson fluid nanofluid in three dimensions using magnetohydrodynamics (MHD). This flow may transport electricity since it is continuous and incompressible. The flow that happens over a long surface is influenced by chemical reactions in addition to heat radiation. By consolidating the non-Newtonian nanofluid into a single state, we used the Williamson fluid model. The basic equations that describe the current fluid's behavior are converted using standard procedures into ordinary differential equations. Finite element analysis is a powerful numerical technique for resolving dimensionless governing equations and validating results that have been previously published. The flow components are verified, scrutinized, and presented in detail to support various flow criterion values. Key factor outcomes are also used as follows:

- Increasing the Hartmann number leads to much better x- and y-axis velocity profiles. Because the magnetic Lorentz force reduces the amount of kinetic energy produced by the flow, it follows that the frequency of interruptions is reduced as well.
- The concentration distribution becomes more constrained as the homogeneous response parameter is raised.
- The relative impact of the two sets of Brownian parameters does not diminish with time; yet, both sets do affect the nanoparticle volume fraction. And yet, there was a marked change in both the temperature and the heat transfer rate through the wall.

- A rise in fluid temperature occurs during thermophoresis as a consequence of the nanoparticles' haphazard movement. Thermal radiation also has a role in the thermal expansion that has been shown.
- While characterizing various flow-regulating backgrounds, their impacts on local Nusselt, Sherwood, and skin friction values have been summarized in a table. Finding the Nusselt number is possible only using the Prandtl number. The Nusselt number and the rate of heat transfer by convection are similar.
- This research not only sheds light on the properties of several physical elements that affect nanofluid movement, but it also develops ideas with broad practical applications in engineering, biology, and industry.

References:

[1] Durgarao, R.S. Vijayakumar, R. Vasudeva Murthy, Joint effects of thermophoresis and Brownian motion on the Willamson-nano fluid flow near a non-linear stretching sheet filled by porous medium, Journal of Nanofluid,11(6)(2022) **.** https://doi.org/10.1166/jon.2022.1887.

[2] Durgarao, R.S. Vijayakumar, R. Vasudeva Murthy, Effect of Chemical reaction on hyperbolic tangent Williamson-Nanofluid flow past an exponentially porous stretching sheet: MHD and slip effects, Tuijin Jishu/Journal of Propulsion Technology ISSN: 1001-4055,44(3) (2023).

[3] S. Nadeem, S. Ashiq, M. Ali, Williamson fluid model for the peristaltic flow of chyme in small intestine, Math. Probl Eng. (2012), 10.1155/2012/479087.

[4] L.A. Lund, Z. Omar, I. Khan, Analysis of dual solution for MHD flow of Williamson fluid with slippage, Heliyon, 5 (3) (2019), Article e01345, 10.1016/j.heliyon.2019.e01345.

[5] Hamid, Hashim, M. Khan, M. Alghamdi, MHD Blasius flow of radiative Williamson nanofluid over a vertical plate, Int. J. Mod. Phys. B, 33 (22) (2019).

[6] A. Aldabesh, S.U. Khan, D. Habib, H. Waqas, I. Tlili, M.I. Khan, W.A. Khan, Unsteady transient slip flow of Williamson nanofluid containing gyrotactic microorganism and activation energy, Alex. Eng. J., 59 (6) (2020), pp. 4315-4328, 10.1016/j.aej.2020.07.036.

[7] Hamid Hashim, M. Khan, Transient flow and heat transfer mechanism for Williamson-nanomaterials caused by a stretching cylinder with variable thermal conductivity, Microsyst. Technol., 25 (2019), pp. 3287-3297, 10.1007/s00542-019-04364-9.

[8] T. Salahuddin, M. Khan, T. Saeed, M. Ibrahim, Y.M. Chu, Induced MHD impact on exponentially varying viscosity of Williamson fluid flow with variable conductivity and diffusivity, Case Stud. Therm. Eng., 25 (2021), Article 100895, 10.1016/j.csite.2021.100895.

[9] Bouslimi Jamal, Omri M., Mohamed R.A., Mahmoud K.H., Abo-Dahab S.M., Soliman M.S., MHD Williamson nanofluid flow over a stretching sheet through a porous medium under effects of joule heating, nonlinear thermal radiation, heat generation/absorption, and chemical reaction, Adv. Math. Phys., 2021 (2021).

[10] Kumar Praveen, Yadav Rajendra Singh, Makinde O.D., Numerical study of Williamson fluid flow and heat transfer over a permeable stretching cylinder with the effects of joule heating and heat generation/absorption, Heat Transfer (2023).

[11] Rehman Khalil Ur, Khan Abid Ali, Malik M.Y., Pradhan R.K., Combined effects of joule heating and chemical reaction on non-Newtonian fluid in double stratified medium: A numerical study, Results Phys., 7 (2017), pp. 3487-3496.

[12] Hayat Tasawar, Saeed Yusra, Asad Sadia, Alsaedi Ahmed, Soret and dufour effects in the flow of Williamson fluid over an unsteady stretching surface with thermal radiation, Z. Naturforsch. A, 70 (4) (2015), pp. 235-243.

[13] Rashad Ahmed M., Nafe Mohamed A., Eisa Dalia A., Heat variation on MHD Williamson hybrid nanofluid flow with convective boundary condition and Ohmic heating in a porous material, Sci. Rep., 13 (1) (2023), p. 6071.

[14] Matin M.H., Pop I., Forced convection heat and mass transfer flow of a nanofluid through a porous channel with a first-order chemical reaction on the wall, Int Commun Heat Mass Transf, 46 (2013), pp. 134-141.

[15] Zang C.L., Zheng L.C., Zhang X.X., Chen G., MHD flow and radiation heat transfer of the nanofluid in porous media with variable heat flux and chemical reaction, App Math Model, 39 (1) (2015), pp. 165-181.
[16] Hossain M.A., Alim M.A., Rees D. A. S., Effect of thermal radiation on natural convection over cylinders of the elliptic cross-section, Acta Mech, 129 (1998), pp. 177-186.
[17] Elbashbeshy E.M.A., Eldabe N.T.M., Youssef I.K., Sedki A.M., Effects of pressure stress work and thermal radiation on free convection around a sphere embedded in a porous media with Newtonian heating, Therm Sci J, 22 (18) (2018), pp. 401-412
[18] Sedki A.M., Abo-Dahab S.M., Bouslimi J., Mahmoud K.H., Thermal radiation effect on unsteady mixed convection boundary layer flow and heat transfer of nanofluid over permeable stretching surface through a porous medium in the presence of heat generation, Sci Prog, 104 (3) (2021), pp. 1-19.
[19] Sedki A.M., Effect of thermal radiation and chemical reaction on MHD mixed convective heat and mass transfer in nanofluid flow due to nonlinear stretching surface through a porous medium, Results Mater, 16 (2022), Article 100334.
[20] Manzur M., Khan M., Rahman M., Mixed convection heat transfer to cross fluid with thermal radiation: Effects of buoyancy assisting and opposing flows, Int J Mech Sci, 138 (2018), pp. 515-523.
[21] Qayyum S., Imtiaz M., Alsaedi A., Hayat T., Analysis of radiation in a suspension of nanoparticles and gyrotactic microorganism for rotating disk of variable thickness, Chinese J Phys, 56 (5) (2018), pp. 2404-2423.
[22] T. Hayat, H. Khalid, M. Waqas, A. Alsaedi, Numerical simulation for radiative flow of nanoliquid by rotating disk with carbon nanotubes and partial slip, Comput. Methods Appl. Mech. Eng., 341 (2018), pp. 397-408.
[23] M. Shoaib, M.A.Z. Raja, M.T. Sabir, M. Awais, S. Islam, Z. Shah, P. Kumam, Numerical analysis of 3-D MHD hybrid nanofluid over a rotational disk in presence of thermal radiation with Joule heating and viscous dissipation effects using Lobatto IIIA technique, Alex. Eng. J., 60 (2021), pp. 3605-3619.
[24] M. Al Nuwairan, B. Souayeh, Simulation of gold nanoparticle transport during MHD electroosmotic flow in a peristaltic micro-channel for biomedical treatment, Micromachines, 13 (3) (2022), p. 374.
[25] S. Aman, I. Khan, Z. Ismail, M. Z. Salleh, Impacts of gold nanoparticles on MHD mixed convection Poiseuille flow of nanofluid passing through a porous medium in the presence of thermal radiation, thermal diffusion and chemical reaction, Neural Computing and Applications, 30 (2018), pp. 789-797.
[26] A. Mostafazadeh, D. Toghraie, R. Mashayekhi, O. A. Akbari, Effect of radiation on laminar natural convection of nanofluid in a vertical channel with single-and two-phase approaches, Journal of Thermal Analysis and Calorimetry, 138 (1) (2019), pp. 779-794.
[27] I. C. Liu, H. I. Andersson, Heat transfer over a bidirectional stretching sheet with variable thermal conditions, Int. J. Heat Mass Transf., 51 (2008), pp. 4018-4024.